

# High-Energy Calibration of the Timepix3 Radiation Monitor

by  
Emanuela Revani

Submitted to the Department of Physics  
as part of the module CA-PHY-800 Bachelor Thesis Physics

for the degree of

BACHELOR OF SCIENCE IN PHYSICS

at

CONSTRUCTOR UNIVERSITY BREMEN

May 2025

Authored by:	Emanuela Revani Department of Physics May 20, 2025
Certified by:	Dr. Daniel Prelipcean Applied Physicist, Thesis Supervisor SY-STI-BMI, European Organization for Nuclear Research
Certified by:	Prof. Dr. Veit Wagner Professor of Physics, Thesis Supervisor Department of Physics, Constructor University

## Statutory Declaration

Family Name, Given/First Name	Revani, Emanuela
Matriculation number	30006125
What kind of thesis are you submitting: Bachelor-, Master- or PhD-Thesis	Bachelor-Thesis

### English: Declaration of Authorship

I hereby declare that the thesis submitted was created and written solely by myself without any external support. Any sources, direct or indirect, are marked as such. I am aware of the fact that the contents of the thesis in digital form may be revised with regard to usage of unauthorized aid as well as whether the whole or parts of it may be identified as plagiarism. I do agree my work to be entered into a database for it to be compared with existing sources, where it will remain in order to enable further comparisons with future theses. This does not grant any rights of reproduction and usage, however.

This document was neither presented to any other examination board nor has it been published.

### German: Erklärung der Autorenschaft (Urheberschaft)

Ich erkläre hiermit, dass die vorliegende Arbeit ohne fremde Hilfe ausschließlich von mir erstellt und geschrieben worden ist. Jedwede verwendeten Quellen, direkter oder indirekter Art, sind als solche kenntlich gemacht worden. Mir ist die Tatsache bewusst, dass der Inhalt der Thesis in digitaler Form geprüft werden kann im Hinblick darauf, ob es sich ganz oder in Teilen um ein Plagiat handelt. Ich bin damit einverstanden, dass meine Arbeit in einer Datenbank eingegeben werden kann, um mit bereits bestehenden Quellen verglichen zu werden und dort auch verbleibt, um mit zukünftigen Arbeiten verglichen werden zu können. Dies berechtigt jedoch nicht zur Verwendung oder Vervielfältigung.

Diese Arbeit wurde noch keiner anderen Prüfungsbehörde vorgelegt noch wurde sie bisher veröffentlicht.

20.05.2025



Signature

Date,

# High-Energy Calibration of the Timepix3 Radiation Monitor

by

Emanuela Revani

Submitted to the Department of Physics  
on May 20, 2025

in partial fulfillment of the requirements for the degree of

BACHELOR OF SCIENCE IN PHYSICS

## ABSTRACT

This thesis summarizes the high-energy calibration of the Timepix3 Radiation Monitor - a 300  $\mu\text{m}$  thick hybrid silicon pixel detector - through two dedicated test campaigns consisting of irradiation with hadron beams in the MeV range. The known literature saturation threshold of 600 keV/pixel was experimentally confirmed as  $E_{\text{sat}}[\text{keV}] = [607 \pm 25]$  keV. Assuming perpendicular irradiation, a linear correlation is found between the expected number of pixels per hadron and the deposited energy of the particle. A parameter scan has been performed to further understand the saturation behaviour: the number of energy-saturated pixels from one to 5 pixels and saturation thresholds up to 400 keV/pixel. A 3<sup>rd</sup> order polynomial was used as a high-energy calibration function to reconstruct the 'missing' measured energy due to saturation.

This extends the detector's usability beyond the linear calibration regime, leading to performance optimization in the radiation field measurements at the CERN accelerator complex.

# Contents

<b>1</b>	<b>Introduction</b>	<b>6</b>
<b>2</b>	<b>Theoretical Background</b>	<b>8</b>
2.1	Particle Stopping Power . . . . .	8
2.1.1	Rationale . . . . .	8
2.1.2	Bohr’s Classical Derivation . . . . .	8
2.1.3	Quantum Mechanical Bethe-Bloch Relation . . . . .	11
2.1.4	The Bragg Curve . . . . .	11
<b>3</b>	<b>Timepix3 Radiation Monitor</b>	<b>13</b>
3.1	Technical Background . . . . .	13
3.1.1	Detector Construction . . . . .	13
3.1.2	Operational Principle . . . . .	13
3.1.3	Timepix3 Clustering and Capabilities . . . . .	15
3.1.4	Detector Bias Settings . . . . .	16
<b>4</b>	<b>Experimental Set-Up</b>	<b>17</b>
4.1	CNA . . . . .	17
4.2	Partially Depleted Detector Configuration . . . . .	17
4.3	Fully Depleted Detector Configuration . . . . .	18
4.3.1	Particle Irradiation Energies . . . . .	19
4.3.2	Energy Calibration . . . . .	20
4.4	Particle Range in Matter . . . . .	20
<b>5</b>	<b>Data Analysis Results</b>	<b>22</b>
5.1	Determination of the Saturation Threshold . . . . .	22
5.2	Fully Biased Detector Data Analysis . . . . .	24
5.2.1	General Sensor Response . . . . .	24
5.3	Configuration Comparison . . . . .	25
5.3.1	Correlation between Cluster ToT and Area . . . . .	25
5.4	High-Energy Calibration . . . . .	27
5.4.1	Algorithm Version 1 . . . . .	28

5.4.2	One Uncalibrated Pixel . . . . .	29
5.4.3	Algorithm Version 2 . . . . .	30
5.4.4	Algorithm Version 3 . . . . .	31
<b>6</b>	<b>Future Directions</b>	<b>33</b>
<b>7</b>	<b>Discussion and Conclusion</b>	<b>34</b>
	<b>References</b>	<b>39</b>

# Chapter 1

## Introduction

The fundamental goal of this thesis is to perform a High-Energy Calibration of the Timepix3 Radiation Monitor [1] in the context of the Radiation to Electronics (R2E) [2] activity at the European Organisation for Nuclear Research (CERN) [3]. The R2E main objectives are two-fold: (i) to develop radiation-resistant electronics systems, and (ii) optimize the performance of the infrastructure in the CERN accelerator complex [4]. To achieve this, the huge radiation levels generated from particle beams are constantly under monitoring [5–7], and new detector technologies are investigated [1, 8].

The new Timepix3 Radiation Monitor has been developed as a suitable candidate for numerous applications within the complex scenarios accross the CERN accelerator complex [9–11], owing to its enhanced capabilities compared to the existing monitoring technologies [12, 13]. A characterization of the response of the Timepix3 sensor in the high-energy regime (MeV range) is necessary, since saturation occurs above up to an energy of 600 keV/pixel [1, 14]. Therefore, the main aim of this work is to extend the known (linear) calibration regime to even higher energies.

To achieve this, two test campaigns have been conducted at Centro Nacional de Acceleradores (CNA) [15] in Sevilla, Spain, by irradiating the Timepix3 with hadron beams in the MeV range. The difference between the two includes altering the applied bias voltage to obtain different depletion volumes - partial in the first case, and full in the other; comparing the two detector configurations is another objective of this work. The amount of energy deposited and the corresponding cluster area formed are examined to determine the spatial spread per amount of charge in both cases. This is essential for differentiating the saturation per cluster among them.

At the final stage, the high-energy calibration is performed. A previously developed algorithm is applied to the data, and the expected deposited energy is distributed: equally (version one); as a ratio of the measured values (version two). A third version involving a third-order polynomial [14] parameters is applied (version three). A parameter scan is done with the count of uncalibrated pixels and thresholds, and the expected deposited energy as a function of the measured deposited energy is displayed.

In chapter 2, the thesis begins by providing a theoretical foundation on the interaction of charged hadrons with matter, described by the Bethe-Bloch equation. Subsequently, in chapter 3, a thorough description of the Timepix3 Radiation Monitor is provided, outlining its construction and operational principle. Chapter 4 describes the experimental set-up in the two test campaigns conducted at CNA. The data analysis results are shown in chapter 5, starting with the determination of the saturation threshold. Lastly, in chapter 6, a summary of the results is presented alongside additional work that can be implemented in the future for the mixed radiation field of the Large Hadron Collider (LHC).

# Chapter 2

## Theoretical Background

### 2.1 Particle Stopping Power

#### 2.1.1 Rationale

All charged particles, such as protons and heavy ions, lose energy mainly due to ionization as they penetrate a given material [16]. The rate of energy loss of the ionizing radiation per unit path length traveled is known as the stopping power  $dE/dx$ , or Linear Energy Transfer (LET). When a high-energy charged particle interacts with matter, the corresponding mean kinetic energy loss due to the Coulomb interaction with the electrons of the medium can be described by the Bethe-Bloch equation [17].

Here, a classical derivation of the stopping power by Niels Bohr is introduced first. Afterwards, the quantum mechanical expression derived by Hans Bethe and Felix Bloch is presented [18].

#### 2.1.2 Bohr's Classical Derivation

An example collision, taking into consideration that the mass of the incident particle is much larger than the mass of the electron ( $M \gg m_e$ ), with the latter assumed to be at rest since the interaction time is much lower than the respective orbital motion, is shown in Fig. 2.1.

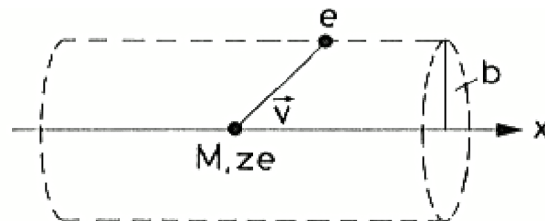


**Figure 2.1.** Diagram from Ref. [19], representing the example interaction between an incident particle and an electron in the material. A cylindrical Gaussian surface is drawn for the momentum transfer calculation.



Assume a particle with charge  $ze$  and velocity  $\vec{v}$ , a target electron with charge  $e$ , and an impact parameter  $b$ , i.e., the transverse distance between the direction of the particle's motion and the center of the target. Eventually, the momentum transfer during the inelastic collision with the electron can be calculated as:

$$\Delta \vec{p}_\perp = \int \vec{F}_\perp \cdot dt = \int e \vec{E}_\perp \cdot dt \quad (2.1)$$

Only the perpendicular component of the electric field  $\vec{E}_\perp$  has an impact since  $\vec{E}_\parallel$  cancels out due to symmetry. Additionally, by using Gauss' law [18]:

$$\int \vec{E} \cdot d\vec{A} = \frac{Q}{\epsilon_0} \quad (2.2)$$

$$\int E_\perp \cdot 2\pi b dx = \frac{ze}{\epsilon_0} \quad (2.3)$$

where  $\epsilon_0$  is the permittivity of free space and  $b$  is called the impact parameter as seen in Fig. 2.1. Analogously, by comparing Equation 2.1 and 2.3 and rewriting  $dt$  as  $\frac{dx}{v}$ , the final expression for the momentum transfer  $\Delta p_\perp$  becomes:

$$\Delta p_\perp = \frac{1}{4\pi\epsilon_0} \cdot \frac{2ze^2}{bv} \quad (2.4)$$

One can also compute the energy that is transferred to the target electron, for an impact parameter  $b$ , by the following relation.

$$\Delta E = \frac{\Delta p_\perp^2}{2m_e} = \frac{1}{(4\pi\epsilon_0)^2} \cdot \frac{2z^2e^4}{b^2v^2m_e} \quad (2.5)$$

Thereafter, let us consider a cylindrical shell with a volume element  $dV = 2\pi b \cdot db \cdot dx$  as outlined in Figure 2.2 and the electron number density  $n_e = N_A \cdot \rho \cdot Z/A$ , where  $\rho$  is the mass density of the material,  $Z$  is the atomic number, and  $A$  the atomic mass.

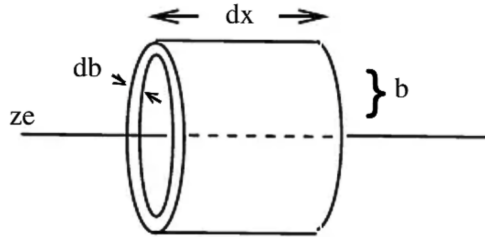


**Figure 2.2.** Diagram from Ref. [19] of the cylindrical shell with an impact parameter  $b$ .

Then, the number of electrons in the target at any value of the impact parameter  $b$  is:

$$N_e = n_e \cdot 2\pi b \cdot db \cdot dx \quad (2.6)$$

Hence, the energy loss by the incident particle due to a path length  $dx$  for a distance between  $b$  and  $b + db$  in the material is:

$$-dE(b) = \Delta E \cdot N_e = \frac{4\pi n_e z^2 e^4}{m_e v^2} \cdot \frac{db}{b} \cdot dx \quad (2.7)$$

Subsequently, the impact on all electrons in the target needs to be computed. Dividing both sides by  $dx$  and computing the integral over the impact parameters  $b_{min}$  and  $b_{max}$ :

$$-\frac{dE}{dx} = \frac{4\pi n_e z^2 e^4}{m_e v^2} \cdot \int_{b_{min}}^{b_{max}} \frac{db}{b} = \frac{4\pi n_e z^2 e^4}{m_e v^2} \cdot \ln \left( \frac{b_{max}}{b_{min}} \right) \quad (2.8)$$

A suitable range includes that  $b_{min} > \lambda_e$  where  $\lambda_e$  is the de Broglie wavelength; from the Heisenberg uncertainty principle, impact parameters below this are irrelevant. To compute this variable, one has to consider that the minimum distance gives the maximum energy transfer from Equation 2.5. Therefore, a head-on collision will transfer:

$$\Delta E = \frac{1}{2} \gamma^2 m_e v^2 = \frac{2z^2 e^4}{m_e b^2 \beta^2 c^2} \quad (2.9)$$

where  $\gamma = (1 - \beta^2)^{-1/2}$  and  $\beta = v/c$ . Finally,  $b_{min}$  is defined to be:

$$b_{min} = \frac{2ze^2}{\gamma m_e \beta^2 c^2} \quad (2.10)$$

Since  $b_{max}$  is the maximum distance to have a minimum effect of ionizing the shell electrons:

$$\Delta E = I = \frac{2z^2 e^4}{m_e b^2 \beta^2 c^2} \quad (2.11)$$

$$b_{max} = \frac{ze^2}{\beta c} \cdot \sqrt{\frac{2}{m_e I}} \quad (2.12)$$

where  $I \sim h < \nu_e >$  is the effective ionization. Altogether, Bohr's classical description of energy loss with distance can be written as:

$$-\frac{dE}{dx} = \frac{4\pi z^2 e^4}{m_e \beta^2 c^2} \cdot n_e \cdot \ln \left( \frac{m_e \gamma^2 \beta^2 c^2}{2I} \right) \quad (2.13)$$

This expression deviates from the quantum mechanical formulation by a factor of 2, which takes into account the spin of the electrons as well.

### 2.1.3 Quantum Mechanical Bethe-Bloch Relation

The bridging between the classical and quantum models has been done by Bethe and Bloch, providing the following more accurate relation for the mean kinetic energy loss due to the interaction of particles with matter.

$$-\left\langle \frac{dE}{dx} \right\rangle = K z^2 \frac{Z}{A} \frac{1}{\beta^2} \left[ \frac{1}{2} \ln \left( \frac{2m_e c^2 \beta^2 \gamma^2 W_{\max}}{I^2} \right) - \beta^2 - \frac{\delta(\beta\gamma)}{2} \right] \quad (2.14)$$

where  $\mathbf{z}$  is the charge of the incident particle,  $\mathbf{I}$  is the mean excitation energy,  $\mathbf{K} = 4\pi N_A r_e^2 m_e c^2$  ( $N_A$ : Avogadro's Number,  $r_e$ : electron radius,  $m_e$ : electron mass),  $\delta(\beta\gamma)$  is the density correction to ionization energy loss (the distant electrons from the trajectory of the particle have a lower effect because of the relatively lower electric field), and  $\mathbf{W}_{\max} = \frac{2m_e c^2 \beta^2 \gamma^2}{1+2\gamma m_e/M+(m_e/M)^2}$  is the maximum energy transfer (direct head-on collision of the charged particle with an electron).

To summarize, for charged particles, the stopping power is directly proportional to the particle's charge squared and inversely proportional to the square of its velocity. Consequently, since alpha particles have double the charge of protons, their stopping power is relatively higher.

### 2.1.4 The Bragg Curve

As an incident charged particle interacts with the material and goes through, it loses energy and deposits it along the way due to the continuous interactions with the existing electrons [18]. The total stopping power due to electronic and nuclear interactions in Silicon as a function of the kinetic energies of incident protons is displayed in Fig. 2.3.

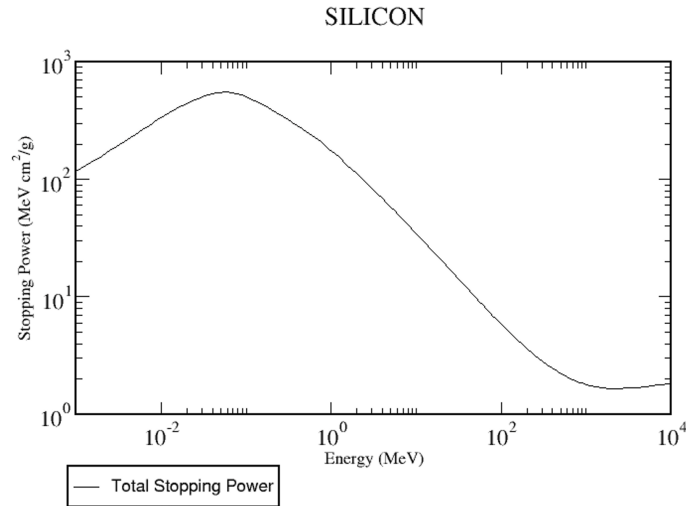


**Figure 2.3.** The total stopping power  $dE/dx$  for protons with different energies, in Silicon. Data taken from Ref. [20].

In the energy range relevant for the test campaigns described in Section 4, the charged hadron primarily loses its energy at a relatively slower rate. However, as it further travels across and slows down, the rate of energy loss increases until it reaches a maximum immediately before the particle stops. This notable rise in the energy deposition at the end of the particle's range is called the Bragg Peak. However, for very high energies (in the GeV range), the behavior gets reversed. Due to the reduced interaction time of higher energy protons with the residual electrons in the material, the stopping power decreases with increasing kinetic energy, which results in a higher particle range in the material.

The deposited energy for stopping charged particles relative to the distance through the material can be described by a Bragg curve. Different proton energies are shown in Figure 2.4, as simulated using the FLUKA Monte Carlo code [21–23], to thoroughly analyze the energy loss rate as they penetrate through the silicon sensor. To further detail, consider the following example. The difference in depth for the two beam energies of 2070 keV and 3000 keV is approximately 50  $\mu\text{m}$ . Nevertheless, for a similar energy difference, the two beam energies of 4997 keV and 6000 keV, the difference in depth results in around 100  $\mu\text{m}$ . This example confirms that higher-energy particles penetrate much deeper with less energy loss. Particles in this regime are the so-called Minimum Ionising Particles (MIPs), and muons represent the most abundant particle species at the CERN accelerator complex that manage to escape the location where they have been generated.

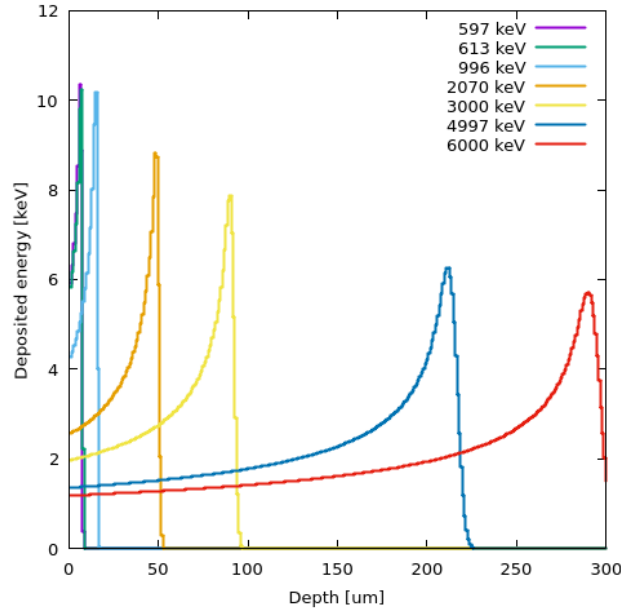


**Figure 2.4.** Deposited energy as a function of depth in Silicon for various proton energies.

In addition, according to the Bethe-Bloch equation, the stopping power at lower energies is inversely proportional to the square of the velocity, which is why the Bragg Peak takes place just before the particle's velocity approaches zero. Hence, before it stops, more energy is deposited per distance traveled, and therefore, more ionization occurs.

# Chapter 3

## Timepix3 Radiation Monitor

The Timepix3 detector technology [12, 13, 24] has a wide range of applications - from medicine to research, some of which potentially include radiation therapy [25], coloured X-ray imaging [26], electron microscopy [27], and radiation characterization in space [28]. A thorough analysis of the construction and operational principles of the detector relevant to this thesis is provided in the following sections.

### 3.1 Technical Background

#### 3.1.1 Detector Construction

The Timepix3 [13] chip has been developed as a next-generation hybrid pixel detector based on a readout Application-Specific Integrated Circuit (ASIC). It has been developed by the Medipix3 Collaboration [24] at CERN, as a successor to the Timepix [12]. The chip itself used in the Timepix3 RadiationMonitor was produced by ADVACAM [29], Prague, Czech Republic.

From a technical perspective, the Timepix3 is a p-in-n Silicon detector, composed of  $256 \times 256$  pixels with a pixel pitch of , resulting in an active sensor area of  $1.98 \text{ cm}^2$ . The semiconductor sensor can be of various materials such as Si, GaAs, CdTe, SiC, etc, and of various thicknesses from 100 to 1000  $\mu\text{m}$ . A minimum semiconductor layer thickness of 300  $\mu\text{m}$  is essential for particle identification [30]; therefore, the silicon layer in the Timepix3 Radiation Monitor is designed to be at least this thickness. In addition, the connection of the active sensor layer to the ASIC chip is done through bump-bonding, which gives the Timepix3 properties of a hybrid detector.

#### 3.1.2 Operational Principle

To outline, the Timepix3 Radiation Monitor operates in hole collection mode since the silicon sensor is p-doped. When ionizing particles interact with the sensor material of the detector, electron-hole pairs are generated from ionization. The free charge carriers are therefore collected

through the pixels' electrodes in the presence of the electric field  $\vec{E}$  caused by the application of the specific bias voltage  $V_{bias}$ . The amount of these collected charge carriers is proportional to the energy deposited by the incoming radiation in each pixel. A constant current  $I_{krum}$  (called Krummenacher current) is then applied to discharge the collected charges from the electrodes.

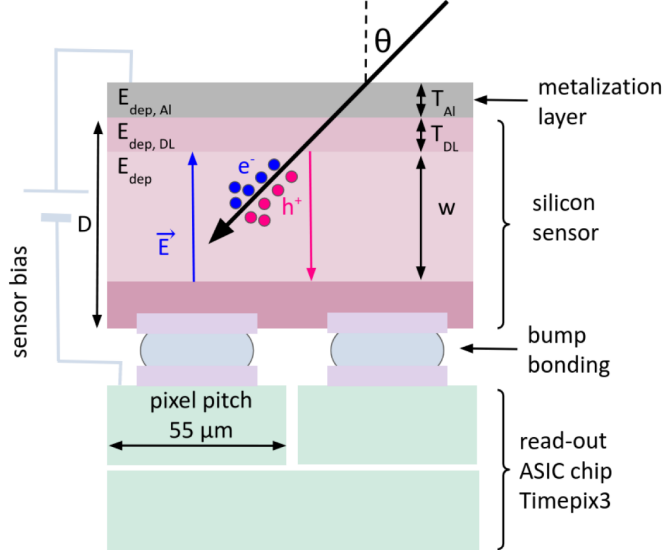


**Figure 3.1.** The Timepix3 detector layout as in the partially biased configuration with the active layer of  $250\ \mu\text{m}$  thickness, aluminum metalization layer, and the dead layer. The sensor is connected to the read-out ASIC chip through bump-bonding. The direction of the electric field  $\vec{E}$  as well as of the charge collection is further indicated. Figure from Ref. [1]

The signal is processed into Time-over-Threshold (ToT) and Time-of-Arrival (ToA). To illustrate, the operational principle of the ToT and ToA for each particle hit is shown in Figure 3.2.

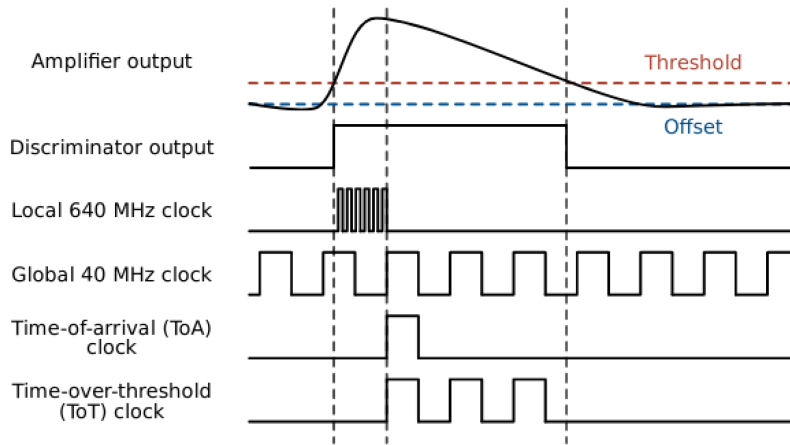


**Figure 3.2.** The amplifier output curve along with the minimum threshold and operation of the 40 MHz and 640 MHz clocks for measuring the ToA and ToT signal of each particle interacting with the detector. Figure from Ref. [1]

1. The **ToT** measures the energy deposited by the particle in each pixel and is proportional to the number of charge carriers that are collected. This charge accumulation causes a signal that, upon exceeding a predefined threshold, drives a 40 MHz global clock which measures the time taken from the triggering (which occurs on the first rising edge of the clock) until it falls below the threshold. This is measured in 25 ns units and stored in 10 bits, therefore, it goes up to  $2^{10} = 1024$  units.
2. The **ToA** records the timing of the particle interaction. When the signal exceeds the threshold, a 640 MHz local clock starts, determining the fast time-of-arrival (fToA) with a precision of 1.5625 ns which is stored in 4 bits and goes up to  $2^4 = 16$  units. This clock runs until the next rising edge of the 40 MHz global clock with a period of 25 ns, at which the ToA is registered, providing a high-resolution timestamp for the event. The latter is stored in 18 bits and goes up to 262144 units. If deployed in the Large Hadron Collider, this nominal clock time of the Timepix3 matches the LHC bunch spacing of 25 ns, for which primary collision products traveling at the speed of light are expected to be observed with regular patterns, while secondary products from other sources (e.g. background radiation from the LHC tunnel) should be more stochastic.

The Timepix3 innovative feature compared to the previous generations (Timepix and Timepix2) is the ability to provide simultaneous time (ToA) and energy (ToT) information. From the detector's dimensions, the total number of pixels is 65536, which are all read independently of each other. The Timepix3 Radiation Monitor is operated in data-driven mode, to accurately identify the signal from each particle that interacts with the detector and to further generate the respective clusters.

### 3.1.3 Timepix3 Clustering and Capabilities

From the interaction of individual particles with the detector, clusters are created, i.e., multiple pixels registering a non-zero ToT. The clusters occur:

1. due to particles entering the detector at an angle, causing them to pass through several adjacent pixels as they traverse the detector plane
2. or the charge carriers generated by the particle's interaction diffusing and spreading to neighboring pixels before the pixel electrodes collect them,

or both. Overall, due to its good timing resolution, Timepix3 is able to accurately measure single-particle hits, given high flux rates (up to  $10^7$  particles/cm<sup>2</sup>s) from the collisions, and detect the direction of the incoming particles.

### 3.1.4 Detector Bias Settings

For this particular analysis, two test campaigns [31, 32] have been performed with the Timepix3 detector operated at different biasing conditions. The depletion volume thickness  $W$  as a function of the bias voltage  $V_{\text{bias}}$  is given by the following relation as described in Ref. [33]:

$$W \approx \sqrt{\frac{2\varepsilon_0\varepsilon_{\text{Si}}}{eN_D}V_{\text{bias}}}, \quad (2.27)$$

where  $\varepsilon_0$  is the permittivity of free space,  $\varepsilon_{\text{Si}}$  is the relative permittivity of Silicon, and  $N_D$  is the donor atom concentration. The numerical values are given in Table 3.1, as theoretically expected from Eqn. 2.27.

**Table 3.1.** The applied bias voltage  $V_{\text{bias}}$  along with the depletion thickness  $W$ , for both irradiation campaigns. The second case leads to full depletion.

Test Campaigns [year]	Bias Voltage ( $V_{\text{bias}}$ ) [V]	Depletion Thickness $W$ [ $\mu\text{m}$ ]
2022	50	250
2025	80	300



# Chapter 4

## Experimental Set-Up

To perform the High-Energy Calibration of the Timepix3 Radiation Monitor, two test campaigns were conducted at the Centro Nacional de Aceleradores (CNA) in Seville, Spain, which are presented in detail in the following sections.

### 4.1 CNA

At the Van der Graaf 3 megavolts (MV) Tandem accelerator at CNA, one can have beams of mono-energetic hadrons (protons, alphas, and heavier ions) up to 6 MeV/n [15]. This facility is mainly used for studying and modifying materials by using ion beam analytical techniques and ion implantation, and characterizing and developing radiation detectors [34].

### 4.2 Partially Depleted Detector Configuration

The first calibration campaign was carried out in February 2022 with protons in an energy range of 0.6 – 5 MeV and alpha particles in an energy range of 1 – 5.6 MeV [31]. For this test campaign, a bias voltage of  $V_{\text{bias}} = 50 \text{ V}$  leading to a partial depletion volume thickness of 250  $\mu\text{m}$  has been applied. At these energy ranges, the incoming radiation is expected to fully stop within the depleted layer of the silicon sensor. To outline, when protons are irradiated perpendicularly towards the detector, they reach the thickness of the active layer at a beam energy of approximately 5 MeV. If higher energies are used, this may lead to a considerable energy deposition of the particles in the non-depleted layer of the silicon. If high enough, the particles can even traverse the entire pixel thickness without stopping. Therefore, the energy range for protons and alphas used for the calibration is intentionally selected to prevent the particles from exceeding the respective depleted layer thickness.

Operating the Timepix3 sensor at partial bias voltage results in an increase in charge sharing to nearby pixels. This occurs as a result of the relatively lower electric field present in the depleted

region, which increases the charge collection time. If more time is needed to collect the charges, then more charge diffusion to neighboring pixels (lateral spread) takes place. As a consequence, the signal magnitude of the collected charge in the incident pixel(s) is reduced as the energy deposited gets distributed over a larger area, thus lowering the saturation per cluster. However, this method is likely to experience more charge recombination due to the slower collection of the charges by the electrodes, which can cause the electron-hole pairs to neutralize each other before being measured.

### 4.3 Fully Depleted Detector Configuration

Another calibration campaign has been performed at the same facility in February 2025, by irradiating the Timepix3 with mono-energetic proton beams with energy range of 0.6–2.2 MeV [32]. A full depletion was obtained by applying a bias voltage of  $V_{\text{bias}} = 80$  V theoretically corresponding to a depletion volume thickness equal to the full sensor thickness ( $W = D = 300\text{ }\mu\text{m}$ ). Likewise, the incoming radiation is expected to fully stop within the depleted region. To visualize, the installation of the Timepix3 at the facility is demonstrated in Figure 4.1.

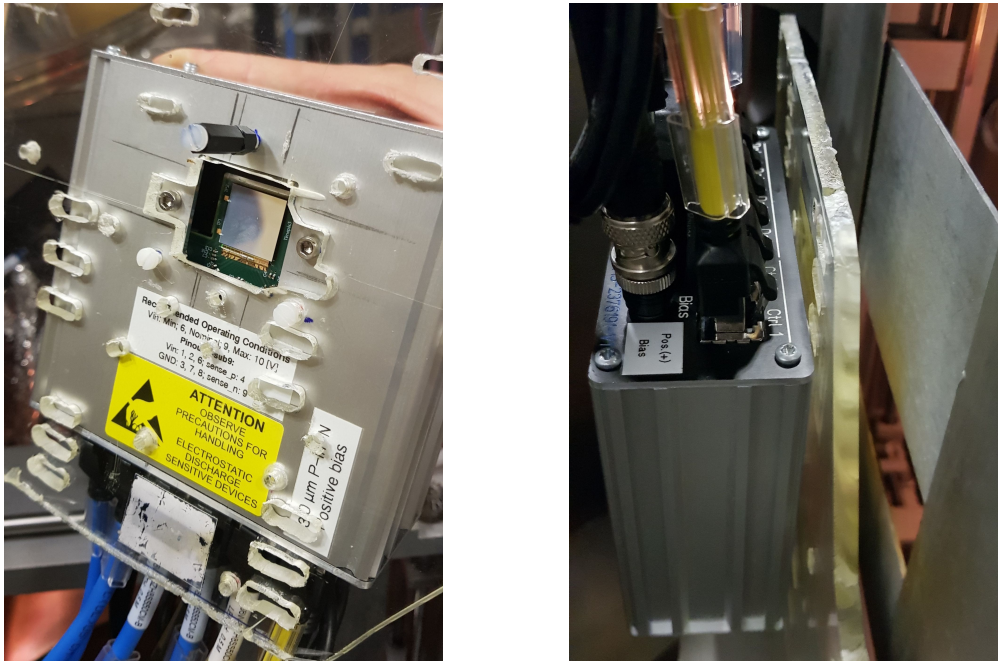


**Figure 4.1.** Installation of the Timepix3 detector at CNA. [32]

Applying a full bias voltage to the detector results in a higher electric field in the depleted region compared to the partially biased case, which causes charges to be collected faster by the electrodes. In other words, the drift velocity is greater since it is directly proportional to the electric field [35]. Considering the charge recombination, due to the shorter lifetime of the charge

carriers - i.e, since they are quickly collected - this process is minimized. Additionally, there is less charge diffusion to adjacent pixels, which leads to smaller cluster areas and higher energy deposited in the main incident pixel(s).

### 4.3.1 Particle Irradiation Energies

A summary table to outline the proton irradiation beam energies used, along with the corresponding portions of the energies that are deposited in the aluminum metalisation layer with thickness  $T_{\text{AL}} = 500 \text{ nm}$  and the dead layer with thickness  $T_{\text{DL}} = 333 \text{ nm}$  is provided below. The energy deposited in the effective layer is then calculated as the difference between the incident beam energy and the energies lost in these top layers.

**Table 4.1.** The table indicates the initial proton beam energy, the energy deposited in the aluminum metalisation layer, the energy deposited in the dead layer, the effective energy in the active layer, and the corresponding relative total energy loss for the fully biased detector configuration. [32]

$E_{\text{beam}}$ [MeV]	$E_{\text{dep,Al}}$ [keV]	$E_{\text{dep,DL}}$ [keV]	$E_{\text{dep,eff}}$ [MeV]	$\Delta E$ [%]
0.593	32	19	0.542	8.6
0.644	30	18	0.595	7.6
0.694	29	17	0.647	6.7
0.743	28	17	0.698	6.0
0.794	27	16	0.751	5.4
0.846	26	15	0.805	4.9
0.943	24	14	0.904	4.1
0.993	23	14	0.956	3.8
1.092	22	13	1.057	3.2
1.192	21	12	1.159	2.8
1.294	20	12	1.262	2.4
1.393	19	11	1.363	2.2
1.494	18	11	1.465	1.9
1.594	17	10	1.566	1.7
1.687	17	10	1.660	1.6
1.798	16	9	1.773	1.4
1.893	15	9	1.868	1.3
1.998	15	9	1.974	1.2
2.099	14	8	2.076	1.1

### 4.3.2 Energy Calibration

Similarly to the partially biased case, the cluster-level energy calibration for converting the ToT into  $E_{\text{dep}}$  has been executed assuming there are no saturation effects. Correspondingly, the mean values of the cluster ToTs as a function of deposited energies in the active layer are plotted and the following equation is obtained.

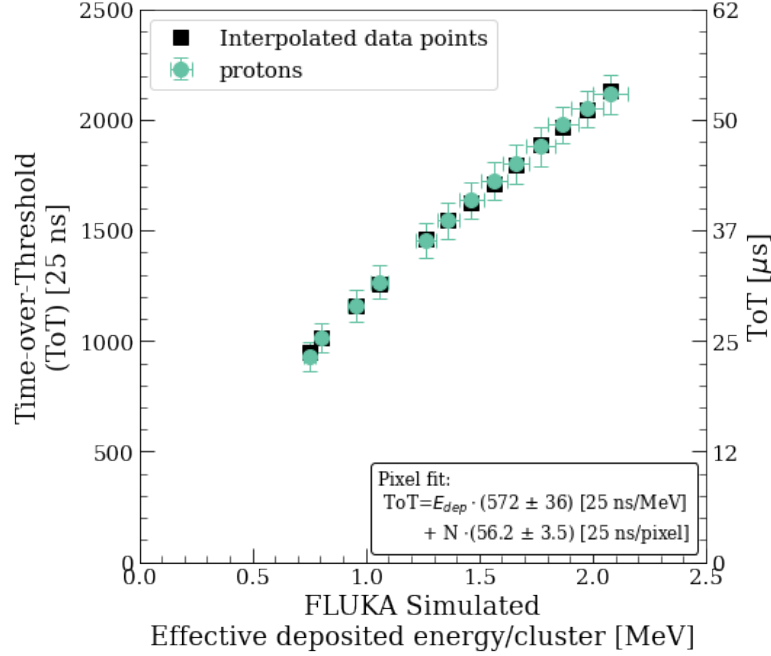


**Figure 4.2.** Timepix3 Radiation Monitor calibration for converting the measured ToT to deposited energy in fully biased configuration. [32]

$$ToT_{\text{reg}}(E_{\text{dep}}) = E_{\text{dep}} \cdot [572 \pm 80 (\sigma_{ToT}) \pm 36 (\sigma_E) \pm 36 (\sigma_{\text{fit}})] \left[ \frac{25 \text{ ns}}{\text{MeV}} \right] + N \cdot [56.2 \pm 3.5 (\sigma_{\text{fit}}) \pm 1.0 (\sigma_{ToT}) \pm 0.4 (\sigma_E)] \left[ \frac{25 \text{ ns}}{\text{pixel}} \right] \quad (4.1)$$

## 4.4 Particle Range in Matter

To determine the particle's range within a material [36], integration through the rate of energy loss from the initial energy  $E$  until it stops can be evaluated as:

$$R = \int_0^E \frac{dE}{dE/dx} \quad (4.2)$$

A graph of the proton and alpha particle range in Silicon along with the stopping power, as functions of their corresponding kinetic energy, is provided in Figure 4.3.

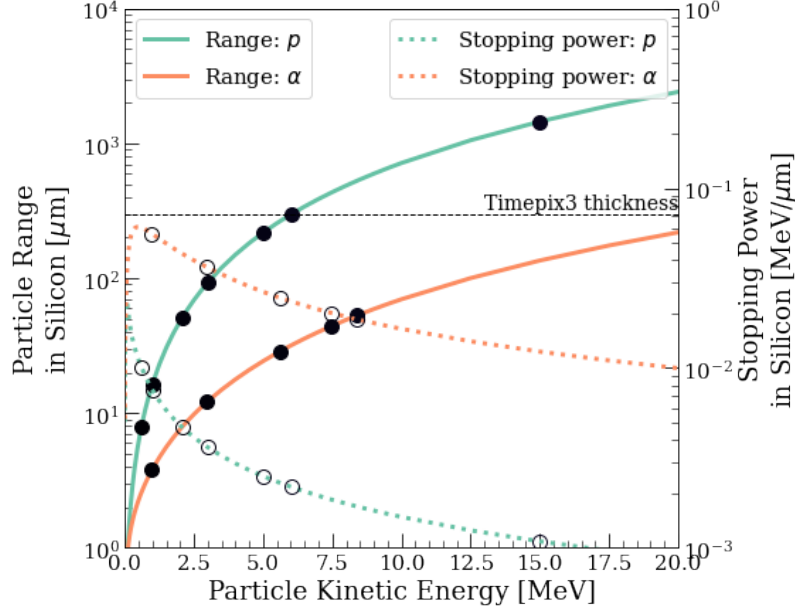


**Figure 4.3.** The range and stopping power of alpha particles and protons in the Silicon sensor of the Timepix3 as a function of their kinetic energy. The horizontal dashed line indicates the detector’s active layer thickness  $D = 300 \mu\text{m}$ .

The range for alpha particles is lower than for protons because of their relatively higher mass and charge. The Timepix3 active Silicon layer thickness boundary shows that the alpha particles fully stop inside, given the specific beam energies. Moreover, protons just reach this thickness at a beam energy of around 5 MeV, considering perpendicular irradiation ( $\theta_i = 90^\circ$ ). For energies higher than this, they are expected to deposit part of their energy in the non-depleted layer of the sensor or even exceed it without stopping.

# Chapter 5

## Data Analysis Results

### 5.1 Determination of the Saturation Threshold

The alpha particle data with beam energies as indicated in Ref. [1] at perpendicular irradiation ( $\theta_i = 90^\circ$ ) has been analyzed. Alphas have a shorter penetration depth than protons, since they have a higher ionization power (i.e., the minimum energy that is required to detach the outermost electron from an atom), which is a result of their relatively higher mass and charge compared to protons.

As outlined in the previous sections, the relation between pixel ToT and the respective deposited energy  $E_{\text{dep}}$  behaves linearly up to an energy deposition of 600 keV per pixel (regardless of detector configuration) and 2 MeV per cluster (for the partially biased case) [1]. For values above these, saturation is expected to take place, resulting in less measured energy deposition than expected. Possible causes for saturation include high-energy depositions, which result in a decrease in the recorded ToT value per pixel.

Hence, to explore these saturation effects, a 2D histogram showcasing the recorded ToT per cluster (determined as the sum of all ToTs of corresponding pixels in the cluster) versus the Cluster Height (the maximum measured pixel ToT for each cluster index) has been plotted in Figure 5.1 Each respective alpha beam energy has been displayed, and a reference line of ( $x = y$ ) has been additionally outlined.

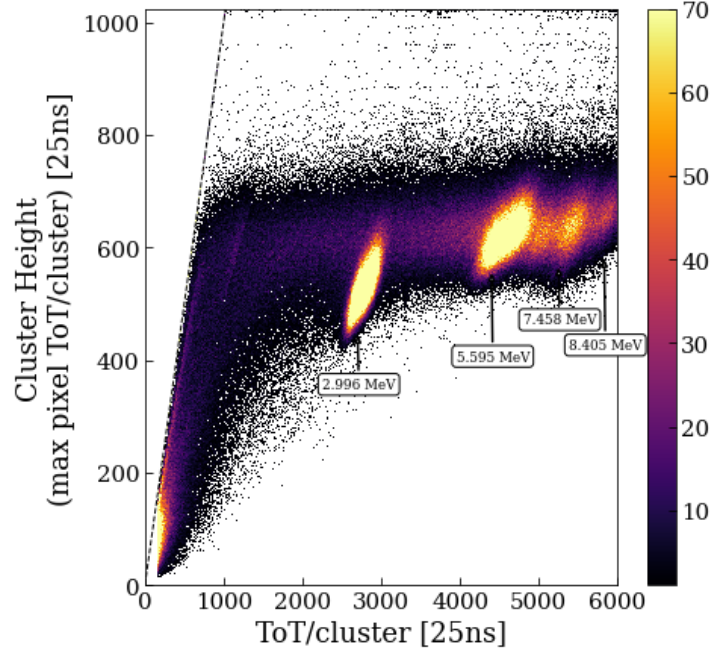


**Figure 5.1.** The maximum pixel ToT as a function of the total ToT per cluster for different alpha beam energies.

Eventually, to quantify the saturation threshold, a projection on the y-axis for incident alphas for the highest beam energies, namely of 5.595 MeV, 7.458 MeV, and 8.405 MeV has been performed, and a Gaussian function was implemented to fit the data. The corresponding histogram for the maximum pixel ToT has been obtained, which is shown in Figure 5.2.

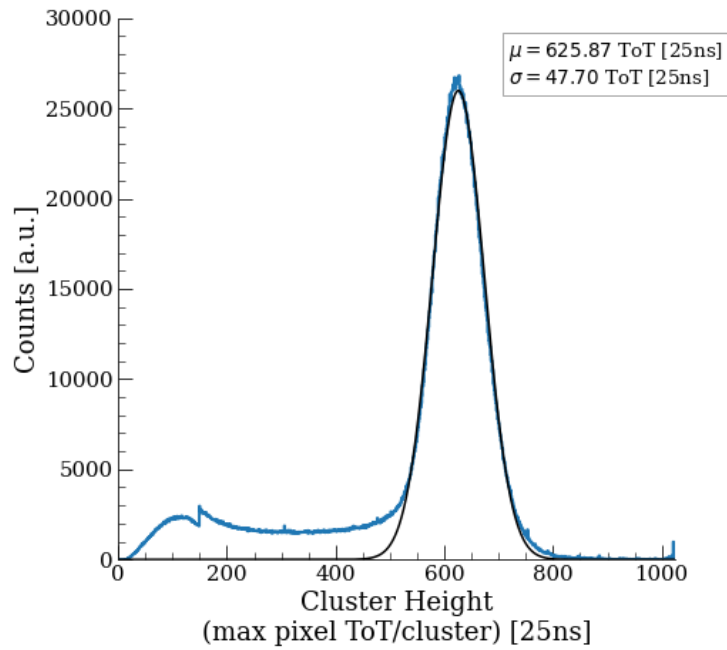


**Figure 5.2.** A projection on the y-axis for Figure 5.1 and the respective Gaussian fit.

The peak corresponds to a ToT value of  $\mu = 626$  ToT [25ns] with a standard deviation of  $\sigma = 48$  ToT [25ns]. Therefore, the saturation threshold determined from the projection on the y-axis of the ToT per cluster versus the cluster height graph was found to be:

$$E_{\text{sat}}[\text{keV}] = [607 \pm 25] \text{ keV}$$

This matches within uncertainties the expected 600 keV limit from literature [14], which further confirms the reliability of the setup.

## 5.2 Fully Biased Detector Data Analysis

### 5.2.1 General Sensor Response

Some exploratory analysis has been primarily implemented in order to understand the behavior of the data when the detector is fully biased. At first, a 1D distribution of the reconstructed clusters' area, i.e., the total number of pixels per cluster, is investigated for several incident beam energies. It is important to mention that only a subset of the total beam energies has been plotted to have a clearer illustration. Therefore, from Figure 5.3, it is evident that with an increase in the deposited energy, the cluster area also increases.

Thereafter, the ToT distribution per cluster, i.e., the sum of all pixel ToTs per respective cluster, has also been plotted for the same beam energies to observe the differences. The result matches the expectation that higher energy depositions result in larger values of the recorded cluster ToT.

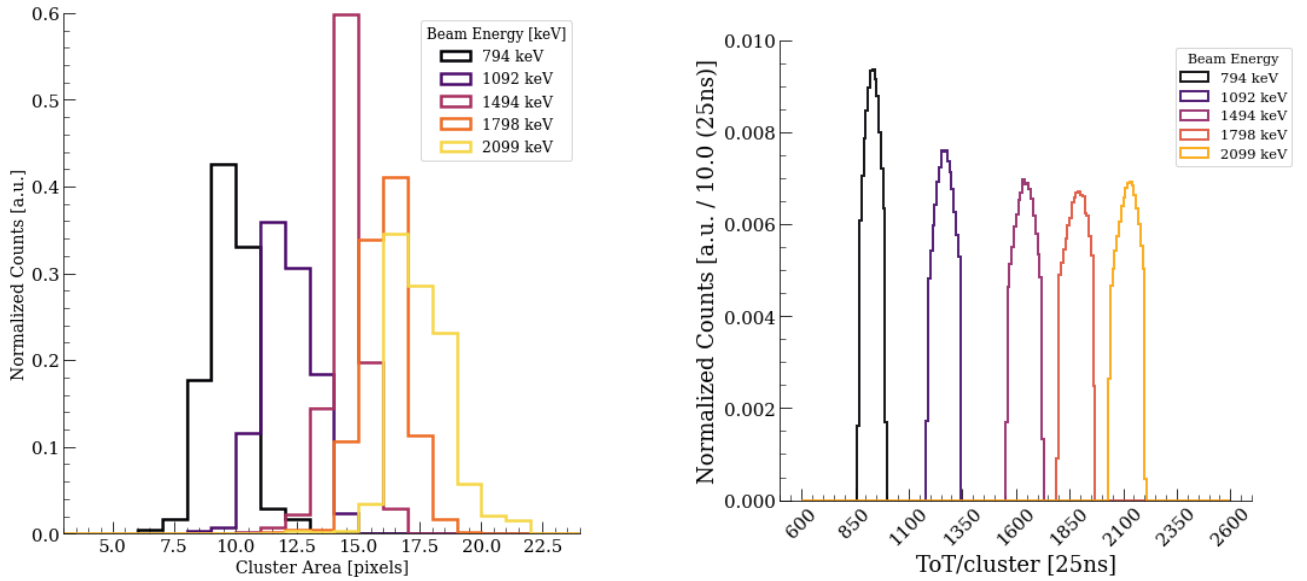


**Figure 5.3.** (Left) 1D distribution of the cluster area and (Right) 1D distribution of the cluster ToT for different proton beam energies.



To further confirm the consistency of the results, the ToT distribution has been plotted on a pixel level for a subset of beam energies as shown in Fig. 5.4. The y-axis is shown on a logarithmic scale to better distinguish the distinct values, and the x-axis can be extended up to 1024 ToT units since this variable is stored in 10 bits. Once more, as the deposited energy increases, the ToT value per pixel gets higher.

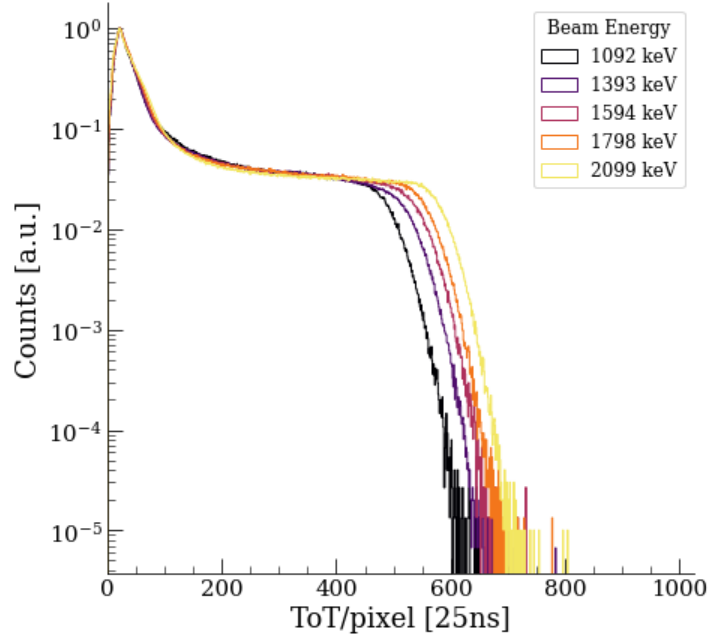


**Figure 5.4.** The ToT distribution per pixel for the distinct proton beam energies.

## 5.3 Configuration Comparison

### 5.3.1 Correlation between Cluster ToT and Area

Subsequently, another cluster-level analysis method has been addressed after verifying how the cluster area, cluster ToT, and pixel ToT operate with regard to changes in the beam energy when being fully biased. Therefore, a 2D histogram of the total ToT per cluster against the cluster area has been plotted, taking into consideration every beam energy in Table 4.1. In addition to this, the respective counts have been normalized by row-wise operations, i.e., dividing each data point by the maximum value in the corresponding row. This is then visualized in Fig. 5.5 (**Left**) for the fully biased configuration.

The same logic has been tested on the partially biased data, considering beam energies up to 2.070 MeV, so as to have the same conditions for an appropriate comparison, as displayed in Fig. 5.5 (**Right**).

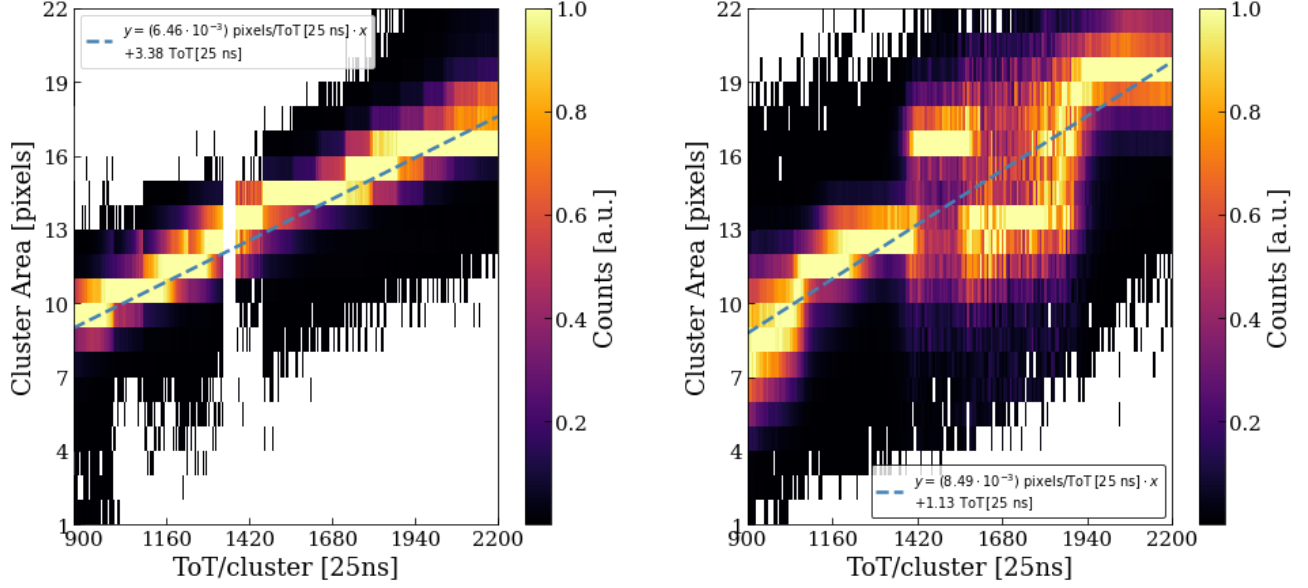


**Figure 5.5.** Comparison of cluster area as a function of ToT per cluster under full (**Left**) and partial (**Right**) bias voltage conditions.

A linear relationship is obtained for both configurations, with the following line equations:

$$y = (6.46 \cdot 10^{-3}) \frac{\text{pixels}}{\text{ToT}[25 \text{ ns}]} \cdot x + 3.38 \text{ ToT}[25 \text{ ns}] \quad (\text{Full Bias}) \quad (5.1)$$

$$y = (8.49 \cdot 10^{-3}) \frac{\text{pixels}}{\text{ToT}[25 \text{ ns}]} \cdot x + 1.13 \text{ ToT}[25 \text{ ns}] \quad (\text{Partial Bias}) \quad (5.2)$$

The slope for the partially biased configuration is higher than for the fully biased one (i.e.,  $m_p > m_f$ ). This indicates that the same amount of energy deposited is distributed among more pixels per cluster for the partially biased case. This is due to the relatively lower electric field  $\vec{E}$  in the depleted region, which leads to slower charge collection and thus, more charge diffusion to adjacent pixels. Therefore, larger cluster areas are created, which results in less saturation as the total charge is shared over more pixels.

Lastly, this analysis provides an alternative method to determine the expected number of pixels per cluster for a given beam energy, but more importantly, how to determine from the number of pixels the total ToT per cluster, which could be undermeasured because of saturation per pixel.

## 5.4 High-Energy Calibration

This part of the analysis aims to perform a per-pixel high-energy calibration by applying a previously developed algorithm [14] to the newly obtained proton data, with the detector being fully depleted as outlined in Section 4.3. It is important to note that the previous study has claimed that this correction factor at high energies can be applied for any Timepix3 detector. The procedure is rather straightforward, for which a demonstration of an example cluster would be extremely useful. In the following figure, a randomly selected cluster created due to irradiation with protons at 0.993 MeV, along with the corresponding ToT of each pixel element, is displayed.

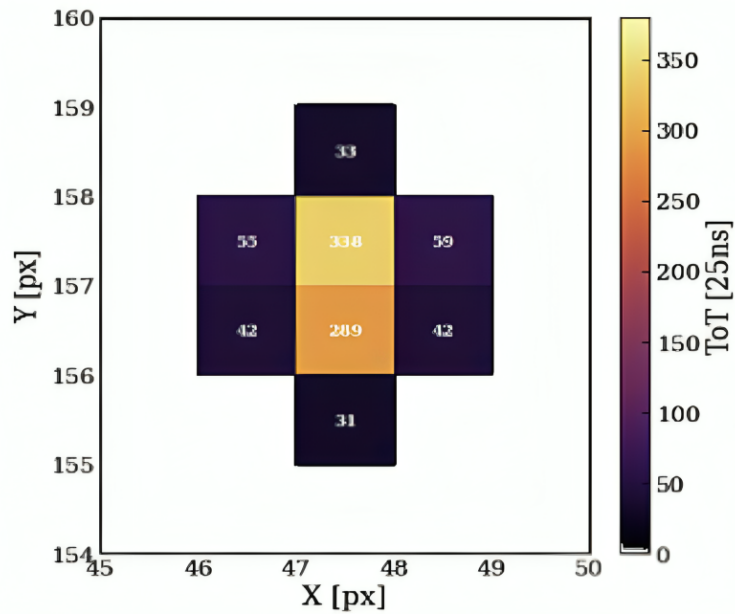


**Figure 5.6.** An example cluster created due to a 0.993 MeV proton along with the ToT measurement in each pixel.

The information that can be extracted from this is the total number of pixels, the distribution of the ToT in each pixel, the total measured ToT, and many others. First and foremost, by knowing the proton beam energy, which in this case is  $E_{\text{beam}} = 0.993$  MeV, the cluster expected ToT that ideally should be recorded by the detector can be calculated by using Equation 4.1.

$$\text{ToT}_{\text{exp}} \approx 1017 \text{ [25 ns]} \quad (5.3)$$

where  $N = 8$  is the total number of pixels. Therefore, the total ToT expected for this cluster is about 1017 [25 ns]. To confirm if this is the case, all ToTs from the individual pixels within the cluster were added up to find the total measured ToT. This results in a value of  $\text{ToT}_{\text{meas}} = 889$  [25 ns], which is lower than what is expected - indicating that saturation has occurred.

To apply a correction, the method aims to initially distinguish between pixels that are below or above a predetermined ToT threshold. For this cluster, if the threshold is assumed at  $\text{ToT}_{\text{thres}} = 150$  keV, it results in six pixels with below-threshold ToT (**calibrated**) and two pixels with above-threshold ToT (**uncalibrated**). To showcase, the uncalibrated pixels have yellow and orange colors in the figure.

After this arrangement, the expected ToT per uncalibrated pixel is determined. To do this, the total ToT of calibrated pixels was found and subtracted from the theoretical  $\text{ToT}_{\text{expected}}$  of the cluster. This is then equally divided among the number of uncalibrated pixels.

$$\text{ToT}_{\text{exp}}^{\text{pixel}} = \frac{\text{ToT}_{\text{exp}}^{\text{cluster}} - \text{ToT}_{\text{cal}}}{N_{\text{uncal}}} \quad (5.4)$$

A sample calculation with the algorithm applied to the cluster in Figure 5.6 is provided in Table 5.1.

**Table 5.1.** Application of the algorithm to an example cluster for determining the expected ToT per uncalibrated pixel.

Variable	Value [25 ns]
$\text{ToT}_{\text{exp}}^{\text{cluster}}$	1017
$\text{ToT}_{\text{meas}}^{\text{cluster}}$	889
$\text{ToT}_{\text{cal}}$	262
$\text{ToT}_{\text{exp}}^{\text{pixel}}$	377.5
$\text{ToT}_{\text{meas}}^{\text{pixel}}$	338 and 289

Ergo, the algorithm suggests that the expected values should be 377.5 [25 ns] for each uncalibrated pixel, but the measured values are both below this value.

#### 5.4.1 Algorithm Version 1

Subsequently, the algorithm has been applied to the entire proton data for the fully biased detector. However, some iterations had to be done with the ToT threshold and the number of uncalibrated pixels, so as not to make any arbitrary assumption. Different numbers of uncalibrated pixels in the [1, 5] range and different ToT thresholds between [150, 400] ToT have been used. Then the algorithm was implemented for every pair (all possible combinations), and the measured versus the expected ToT per uncalibrated pixel has been plotted in Fig. 5.7.

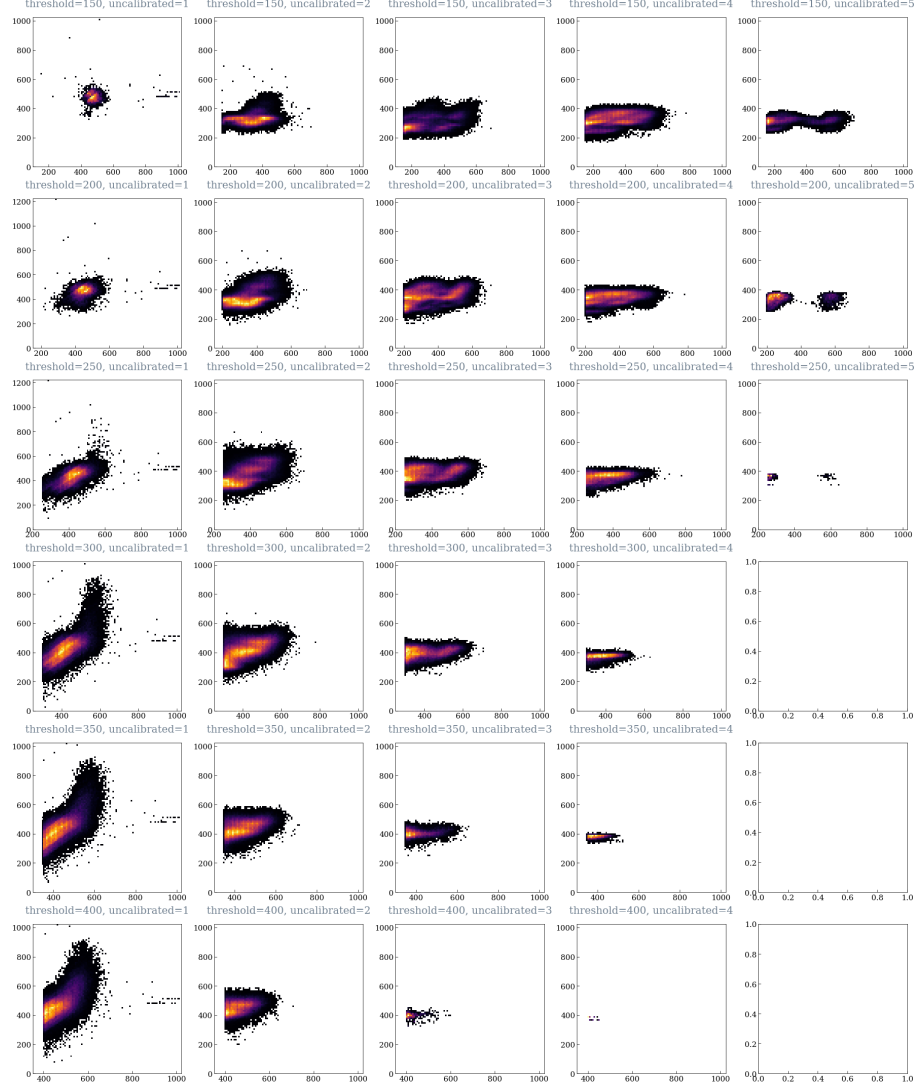


**Figure 5.7.** The measured versus the expected ToT per uncalibrated pixel (equal division) for  $[1, 5]$  uncalibrated pixels and  $[150, 400]$  ToT thresholds for all proton data in fully biased configuration.

In Ref. [14], an arbitrary  $\text{ToT}_{\text{thres}} = 150$  keV has been used, while Figure 5.7 aims to provide a broader picture by performing a parameter scan with different values to improve the algorithm. Nevertheless, this equal distribution of the expected ToT becomes less accurate for  $N_{\text{uncalibrated}} > 2$ . This can be confirmed by the horizontal spread of the data. Therefore, equally assigning the ToT values among  $N_{\text{uncal}}$  requires further consideration.

### 5.4.2 One Uncalibrated Pixel

For the case of only one uncalibrated pixel ( $N_{\text{uncal}} = 1$ ) in the cluster, no assumptions are made regarding the distribution of missing energy amongst the uncalibrated clusters. As such,

a third-order polynomial was fitted to obtain the related parameters. The corresponding plots of the measured versus expected ToT per uncalibrated pixel for  $\text{ToT}_{\text{thres}} = 300$  [25ns], and  $\text{ToT}_{\text{thres}} = 350$  [25ns], are shown in Fig. 5.8a and 5.8b, respectively.

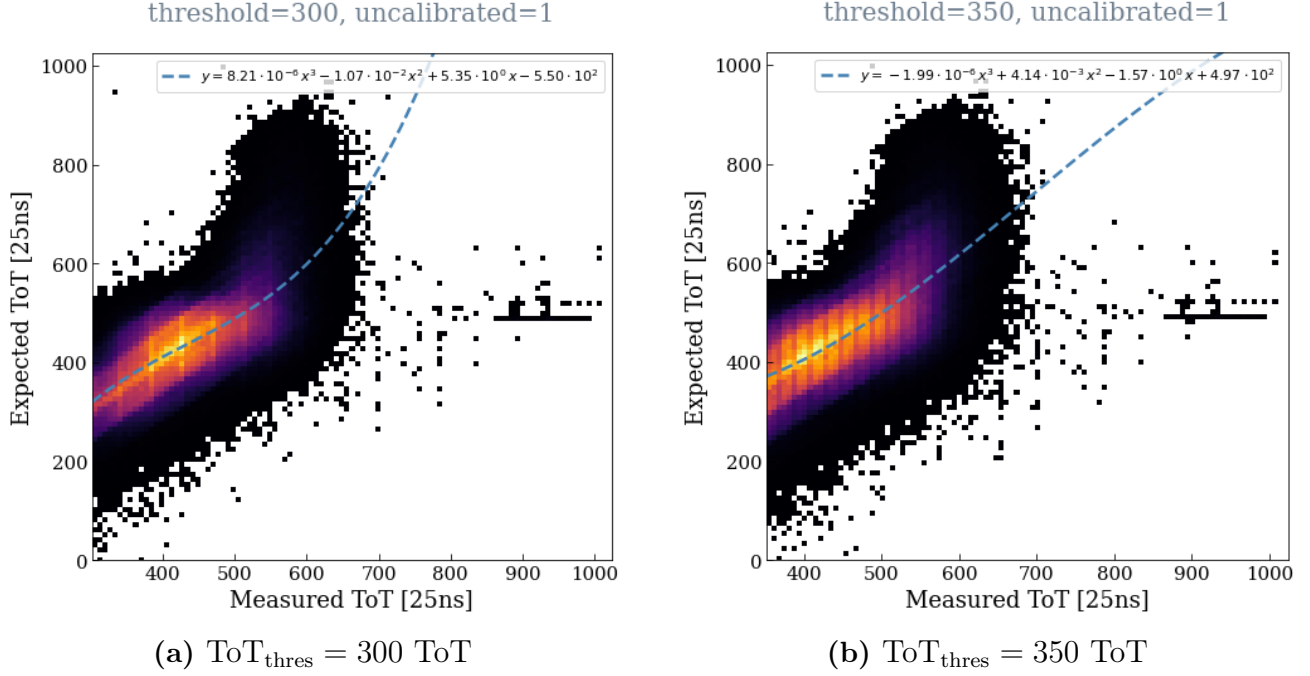


**Figure 5.8.** The measured versus expected ToT for  $N_{\text{uncal}} = 1$  histograms and the corresponding third-order polynomial corrections.

These correction fit parameters can therefore be used to reconstruct the undermeasured energies in the case when only one pixel is saturated due to the incoming radiation.

### 5.4.3 Algorithm Version 2

Another version of the algorithm has been developed - this time, not equal division of the missing ToT amongst the pixels, but a linear distribution. Thus, the total ToT of calibrated pixels was subtracted from the cluster's theoretical  $\text{ToT}_{\text{expected}}$  and divided among the number of uncalibrated pixels based on their  $\text{ToT}_{\text{meas}}$  ratio. Subsequently, this new version has been applied to all clusters for all the beam energies. Once more, different numbers of uncalibrated pixels in the  $[1, 5]$  range and different ToT thresholds between  $[150, 400]$  ToT have been used. The measured versus the expected ToT per uncalibrated pixel has been plotted in Fig. 5.9.

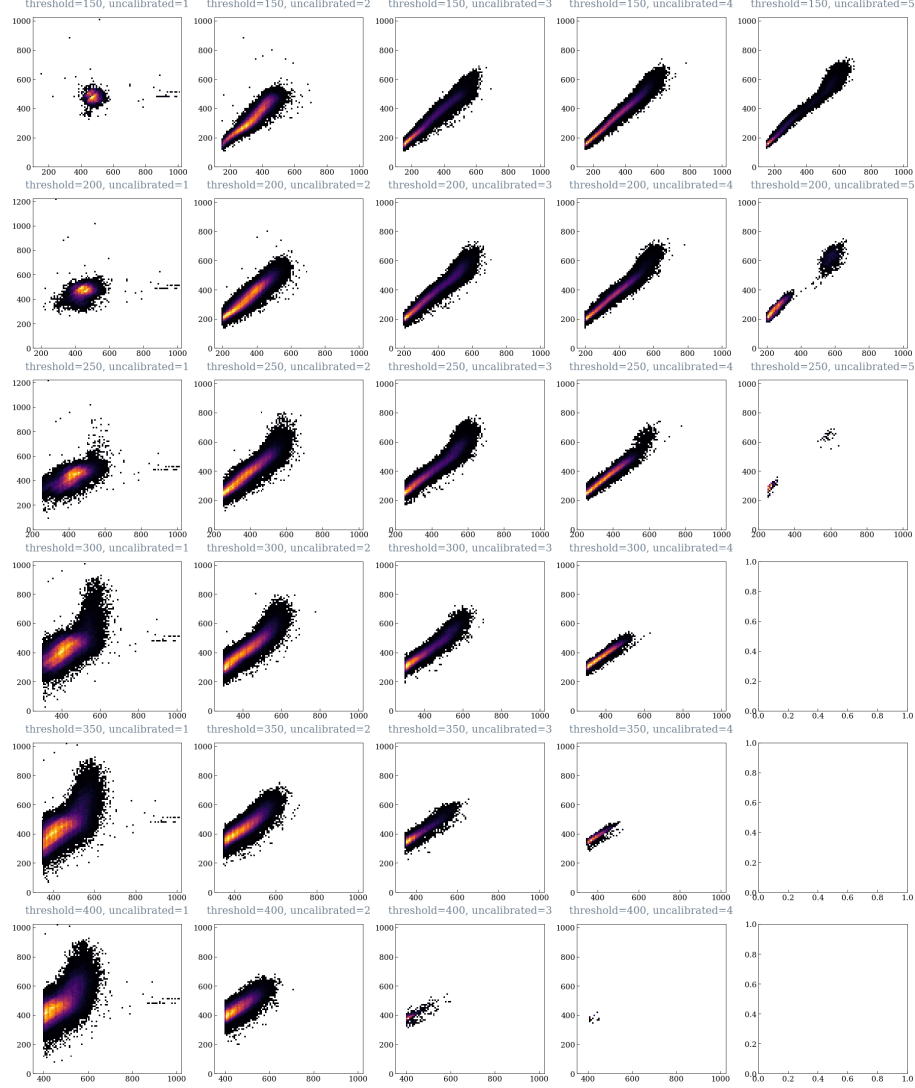


Figure 5.9. Same as Fig. 5.7, but for a linear distribution of the missing energy.

#### 5.4.4 Algorithm Version 3

Given that saturation occurs at energy depositions above 600 keV per pixel, another version has also been implemented with a non-linear distribution of the energy per uncalibrated pixel. The third-order polynomial correction function that has been used was previously determined in Ref. [14] as:

$$f_{\text{corr}}(x) = -1.019 + 1.153 \cdot x - 2.302 \cdot 10^{-3} \cdot x^2 + 9 \cdot 10^{-6} \cdot x^3 \quad (5.5)$$

This function has been applied to all measured energies per uncalibrated pixel to find the corresponding expected energies. The respective 2D histograms are shown in Figure 5.10.



**Figure 5.10.** Same as Fig. 5.7, but for a non-linear distribution of the missing energy.

Saturation effects are evident, since higher energies are expected than measured. Therefore, this non-linear distribution is used as high-energy calibration to reconstruct the 'missing' measured energies due to saturation, extending the detector's usability beyond the linear calibration regime.



# Chapter 6

## Future Directions

To provide an outlook, the higher energy calibration results can now be used to correct the measured energy deposition in any scenario where saturation is present. Within the R2E activity at CERN, there are several planned test campaigns and analyses involving the Timepix3 Radiation Monitor, of which only two are highlighted here:

1. The Timepix3 detector could be used as a beam characterisation monitor for heavy ions as part of the HEARTS [8] project, funded by the European Commission. The ion beam would lead to a signal in the Timepix3 in the very to extremely high energy deposition [37], leading to a known saturation behaviour called the volcano effect [38].
2. An on-going measurement that will suffer from saturation effects is a test campaign on the Quench Protection System (QPS) in the Dispersion Suppressor (DS) region around the ALICE detector [39] (LHC IP2), because of failures of unknown origin that have been observed in the past during the LHC lead ion (Pb) operation. The LET discrimination power of the Timepix3 Radiation Monitor [9] could be used to identify heavy ions in the radiation field.

Outside the R2E activity at CERN, the Timepix3 technology is used in a wide constellation of applications, amongst which those that could be impacted by saturation effects could include radiation monitoring on the International Space Station (ISS) [40], the luminosity measurements and radiation field characterization [30] in the ATLAS detector [41], and the LHCb [42] Timepix3 telescope used for as VERTex reconstruction LOCator (VELO) [43].

# Chapter 7

## Discussion and Conclusion

The radiation environment at the CERN accelerator complex showcases enormous radiation levels, which have to be continuously monitored and mitigated to ensure the successful performance of the experiments, detectors, electronic systems, and other existing units. For this purpose, the Timepix3 Radiation Monitor, a 300  $\mu\text{m}$  hybrid silicon pixel detector based on a readout ASIC, is being heavily tested for integration into this radiation monitoring arsenal. The detector exhibits a linear behavior to the incoming radiation up to an energy of 600 keV/pixel. Within the scope of this thesis, a detailed characterization of the response of the Timepix3 in the high-energy regime (MeV range) has been presented. Upon successful evaluation, this high-energy calibration can be applied to the mixed radiation field data at CERN and correct for the missing measured energy due to saturation.

Two test campaigns have been successfully conducted at Centro Nacional de Acceleradores (CNA) by irradiating the Timepix3 Radiation Monitor with hadron beams in the MeV range at perpendicular irradiation. In the first campaign, a bias voltage of  $V_{\text{bias}} = 50 \text{ V}$  was applied, resulting in a partial depletion volume thickness of  $W=250 \mu\text{m}$ . In the second campaign, the bias voltage was increased to  $V_{\text{bias}} = 80 \text{ V}$ , causing the detector to be fully depleted with a volume thickness of  $W=300 \mu\text{m}$ .

Saturation effects have been identified at high energy depositions, which were observed by the non-linear response of the relation between maximum pixel ToT as a function of the total ToT within each respective cluster. Alpha particles are bombarded at the sensor to quantify the saturation threshold, experimentally determined here at  $E_{\text{sat}}[\text{keV}] = [607 \pm 25] \text{ keV}$ , which is within the range of the expected theoretical 600 keV limit.

Furthermore, the general sensor response for the data when the detector was fully biased has been explored, revealing an increase in the cluster area, cluster ToT, and pixel ToT for the same beam energies compared to the partially biased setup. There is a linear relationship between the cluster area as a function of the deposited energy, in both cases. One can determine the expected number of pixels per cluster for a given ToT signal assuming perpendicular

irradiation, found to be:  $y = [(6.46 \cdot 10^{-3}) \frac{\text{pixels}}{\text{ToT}[25 \text{ ns}]} \cdot x + 3.38 \text{ ToT}[25 \text{ ns}]]$  (partial bias) and  $y = [(8.49 \cdot 10^{-3}) \frac{\text{pixels}}{\text{ToT}[25 \text{ ns}]} \cdot x + 1.13 \text{ ToT}[25 \text{ ns}]]$  (full bias). The variation lies in the slope, i.e.,  $m_p > m_f$ , indicating that the same amount of energy deposited is distributed among more pixels per cluster for the partially biased case. This is due to the relatively lower  $\vec{E}$  in the depleted region, which leads to slower charge collection and thus, more charge diffusion to adjacent pixels (lateral spread). Hence, there is less saturation per cluster as the total charge is shared over a larger area.

The high-energy calibration has been successfully implemented by applying the algorithm to the proton irradiation data on the fully biased configuration. For all versions, a parameter scan was done with the count of uncalibrated pixels and ToT thresholds, and the expected ToT as a function of the measured ToT per pixel was displayed. Version one, i.e., equal distribution of the expected ToT among uncalibrated pixels, proved to be less accurate for  $N_{\text{uncalibrated}} > 2$ , verified by the horizontal spread of the data. However, since no assumption is required on how the ToT should be distributed for the data with only one uncalibrated pixel, a  $3^{rd}$  order polynomial was fitted, and its parameters were obtained.

A second version, with a linear distribution of the expected ToT as a ratio of the measured ToT among the uncalibrated pixels, is more accurate in comparison to version one, but saturation at 600 keV/pixel is expected. For this, Version 3 is implemented, which includes applying a  $3^{rd}$  polynomial with previously defined constants [14] to the measured ToT data per uncalibrated pixel as a non-linear distribution of the energy in order to correct for the missing measured energy due to saturation.

To conclude, applying these correction algorithms to reconstruct the undermeasured radiation levels of the Timepix3 Radiation Monitor leads to performance optimization in the radiation field measurements at the CERN accelerator complex.

# Appendix A

## Total ToT versus Cluster Height for protons

For each configuration of the Timepix3 Radiation Monitor, i.e., partially and fully biased, the proton data at perpendicular irradiation up to 2 MeV are considered, and the total ToT per cluster vs. the maximum pixel ToT is shown below.

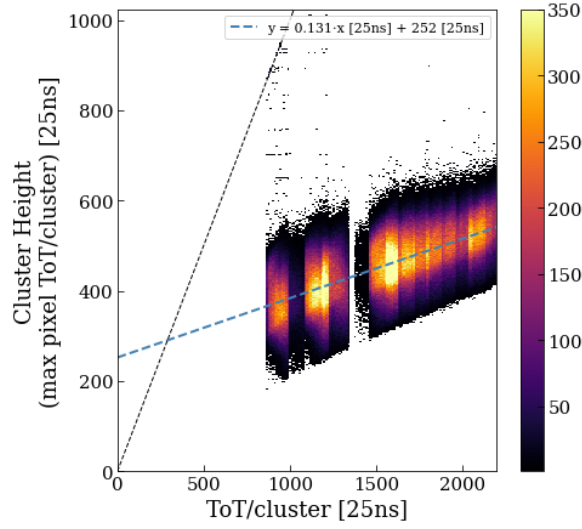


**Figure 7.1.** Total ToT per cluster vs the cluster height for proton data, full bias.

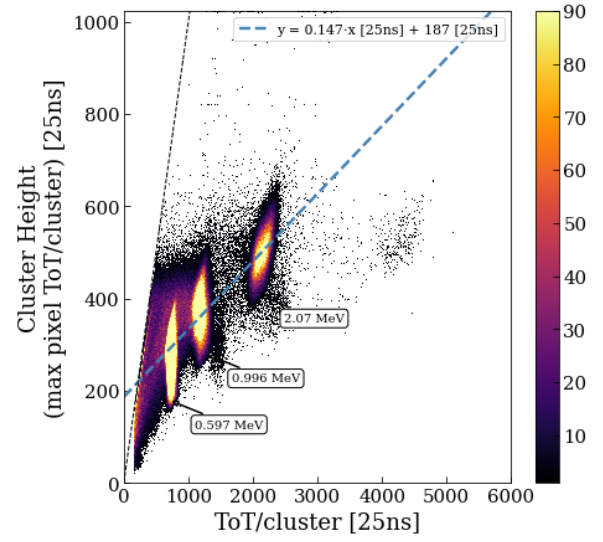


**Figure 7.2.** Total ToT per cluster vs the cluster height for proton data, partial bias.

# Appendix B

## Angular Scan for 6 MeV protons

An angular scan from  $15^\circ$  to  $45^\circ$  with 6 MeV protons is performed for the partially biased configuration, and the total ToT per cluster is plotted against the maximum pixel ToT.

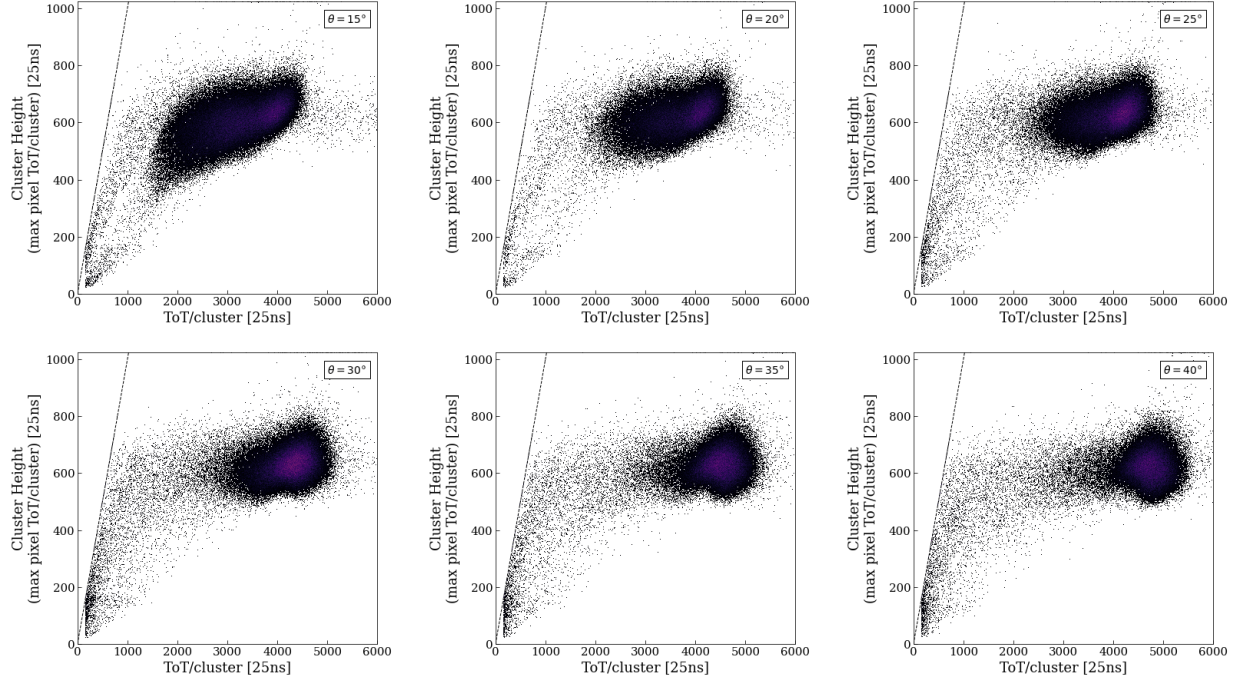


**Figure 7.3.** Total ToT per cluster vs. cluster height for 6 MeV protons at different angles.

# Appendix C

## Analysis on the Time-of-Arrival

The 1D distributions of the ToA per pixel have been plotted to observe the differences in this regard between partially and fully biased configurations. This has been applied to both 1 MeV and 2 MeV proton beam energies, as shown in Figure 7.4 (Left) and Figure 7.4 (Right), respectively.

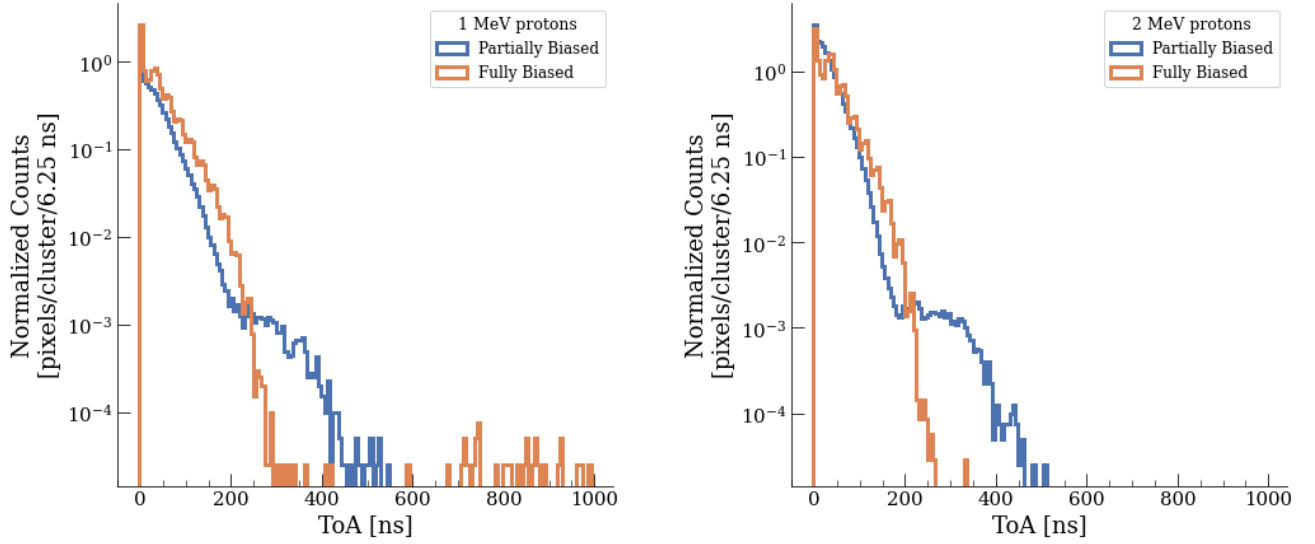


**Figure 7.4.** The ToA distribution per pixel to highlight the differences of the detector at partial and full bias voltage for **(Left)** 1 MeV and **(Right)** 2 MeV proton data.

One can infer that the maximum ToA is lower for the fully biased detector than for the partially biased one. Nevertheless, further analysis is aimed to be conducted to more accurately investigate the measurements on this variable.

# References

- [1] D. Prelicpean et al. “Towards a Timepix3 Radiation Monitor for the Accelerator Mixed Radiation Field: Characterisation with Protons and Alphas from 0.6 MeV to 5.6 MeV”. In: *Applied Sciences* 14.2 (2024). ISSN: 2076-3417. DOI: [10.3390/app14020624](https://doi.org/10.3390/app14020624). URL: <https://www.mdpi.com/2076-3417/14/2/624>.
- [2] *Radiation to Electronics (R2E) at CERN*. Available online: <https://r2e.web.cern.ch/> (Accessed on 10.05.2025).
- [3] CERN. *CERN - European Organization for Nuclear Research*. Accessed: 2025-05-20. URL: <https://home.cern/>.
- [4] *High-Luminosity Large Hadron Collider (HL-LHC): Technical design report*. CERN Yellow Reports: Monographs. Geneva: CERN, 2020. DOI: [10.23731/CYRM-2020-0010](https://doi.org/10.23731/CYRM-2020-0010).
- [5] *Radiation to Electronics (R2E) Monitoring Dashboard*. URL: <https://r2e-monitoring.web.cern.ch> (visited on 07/18/2024).
- [6] K. Bilko et al. “Automated Analysis of the Prompt Radiation Levels in the CERN Accelerator Complex”. In: Proc. 13th International Particle Accelerator Conference (IPAC’22), MOPOMS043 (July 2022), pp. 736–739. DOI: [10.18429/JACoW-IPAC2022-MOPOMS043](https://doi.org/10.18429/JACoW-IPAC2022-MOPOMS043).
- [7] A. Canesse, D. Prelicpean, D. Ricci, D. Di Francesca, G. Lerner, R. Garcia Alia, and S. Danzeca. “Overview of the radiation levels in the CERN accelerator complex after LS2.” In: *14th International Particle Accelerator Conference*. IPAC’23 - 14th International Particle Accelerator Conference IPAC2023.14 (May 2023), pp. 4004–4007. ISSN: 2673-5490. DOI: [doi:10.18429/jacow-ipac2023-thpa046](https://doi.org/10.18429/jacow-ipac2023-thpa046). URL: <https://indico.jacow.org/event/41/contributions/2757>.
- [8] A. Waets et al. “Very-High-Energy Heavy Ion Beam Dosimetry using Solid State Detectors for Electronics Testing”. In: (2024), pp. 1–1. DOI: [10.1109/TNS.2024.3350667](https://doi.org/10.1109/TNS.2024.3350667).
- [9] D. Prelicpean. “Study of the radiation background and of new monitoring tools at the LHC for Run 3 and the HL-LHC.” Presented 30 Jan 2025. 2025. URL: <https://cds.cern.ch/record/2928063>.
- [10] D. Prelicpean, G. Lerner, A. Ciccotelli, F. Cerutti, A. Zimmaro, R. García Alía, and J. Storey. “Measurement of the transversal Muon Rate at the proposed CODEX-b experiment with

- the Timepix3 Radiation Monitor”. In: *16th International Particle Accelerator Conference IPAC2025* (2025). DOI: [10.18429/JACoW-IPAC2025-TUPB004](https://doi.org/10.18429/JACoW-IPAC2025-TUPB004).
- [11] E. Revani, D. Prelicpean, G. Lerner, and J. Storey. “Measurement of the Muon Rate at the SND Experiment with the Timepix3 Radiation Monitor”. In: *16th International Particle Accelerator Conference IPAC2025* (2025). DOI: [10.18429/JACoW-IPAC2025-TUPB005](https://doi.org/10.18429/JACoW-IPAC2025-TUPB005).
  - [12] X. Llopart, R. Ballabriga, M. Campbell, L. Tlustos, and W. Wong. “Timepix, a 65k programmable pixel readout chip for arrival time, energy and/or photon counting measurements”. In: *Nuclear Instruments and Methods in Physics Research Section A: Accelerators, Spectrometers, Detectors and Associated Equipment* 581.1 (2007). VCI 2007, pp. 485–494. ISSN: 0168-9002. DOI: <https://doi.org/10.1016/j.nima.2007.08.079>. URL: <https://www.sciencedirect.com/science/article/pii/S0168900207017020>.
  - [13] T. Poikela et al. “Timepix3: a 65K channel hybrid pixel readout chip with simultaneous ToA/ToT and sparse readout”. In: *Journal of Instrumentation* 9.05 (May 2014), pp. C05013–C05013. DOI: [10.1088/1748-0221/9/05/c05013](https://doi.org/10.1088/1748-0221/9/05/c05013). URL: <https://doi.org/10.1088/1748-0221/9/05/c05013>.
  - [14] R.-E. Mihai, B. Bergmann, and P. Smolyanskiy. “Extending the time-over-threshold calibration of Timepix3 for spatial-resolved ion spectroscopy”. In: (Jan. 2025). arXiv: [2501.04419](https://arxiv.org/abs/2501.04419) [[physics.ins-det](https://arxiv.org/abs/2501.04419)].
  - [15] *Beam Machine Interactions (BMI) at CERN*. Available online: <https://cna.us.es/index.php/en/> (Accessed on 10.05.2025).
  - [16] S. Masciocchi. *Interaction of Particles with Matter - 1*. Lecture slides, GSI and University of Heidelberg. 2017.
  - [17] M. Bindi. *Detector Physics: from particle interactions to tracking concepts*. 2021. URL: <https://indico.cern.ch/event/999261/>.
  - [18] M. Donegà. *INTERACTION OF PARTICLES WITH MATTER*. ETH Zurich. 2019.
  - [19] Cloudylabs. *Lecture 2: Passage of Particles Through Matter*. <https://www.cloudylabs.fr/wp/wp-content/uploads/2019/07/Lecture2.pdf>. 2019.
  - [20] *Stopping-Power & Range Tables for Electrons, Protons, and Helium Ions*. Available online: <https://www.nist.gov/pml/stopping-power-range-tables-electrons-protons-and-helium-ions>.
  - [21] *FLUKA website*. Available online: <https://fluka.cern>.
  - [22] FLUKA.CERN Collaboration. “Overview of the FLUKA code”. In: *Annals of Nuclear Energy* 82 (2015), pp. 10–18. ISSN: 0306-4549. DOI: <https://doi.org/10.1016/j.anucene.2014.11.007>. URL: <http://www.sciencedirect.com/science/article/pii/S0306454914005878>.
  - [23] FLUKA.CERN collaboration. “New Capabilities of the FLUKA Multi-Purpose Code”. In: *Frontiers in Physics* 9 (2022). ISSN: 2296-424X. DOI: [10.3389/fphy.2021.788253](https://doi.org/10.3389/fphy.2021.788253). URL: <https://www.frontiersin.org/article/10.3389/fphy.2021.788253>.
  - [24] *Medipix Collaboration*. Available online: <https://medipix.web.cern.ch/home> (Accessed on 07.05.2025).



- [25] C. Oancea, J. Šolc, C. Granja, E. Bodenstein, F. Horst, J. Pawelke, and J. Jakubek. *Radiation Measurements Using Timepix3 with Silicon Sensor and Bare Chip in Proton Beams for FLASH Radiotherapy*. 2024. arXiv: [2410.00549](https://arxiv.org/abs/2410.00549) [physics.ins-det]. URL: <https://arxiv.org/abs/2410.00549>.
- [26] C. Fröjd. *Applications for vertexing detectors*. 2016. URL: <https://indico.cern.ch/event/452781/>.
- [27] Y. Auad, J. Baaboura, J.-D. Blazit, M. Tencé, O. Stéphan, M. Kociak, and L. H. Tizei. “Time calibration studies for the Timepix3 hybrid pixel detector in electron microscopy”. In: *Ultramicroscopy* 257 (2024), p. 113889. ISSN: 0304-3991. DOI: <https://doi.org/10.1016/j.ultramic.2023.113889>. URL: <https://www.sciencedirect.com/science/article/pii/S0304399123002061>.
- [28] M. Farkas et al. “Characterization of a Large Area Hybrid Pixel Detector of Timepix3 Technology for Space Applications”. In: *Instruments* 8.1 (2024). ISSN: 2410-390X. DOI: [10.3390/instruments8010011](https://www.mdpi.com/2410-390X/8/1/11). URL: <https://www.mdpi.com/2410-390X/8/1/11>.
- [29] Advacam Ltd. Accessed: 2025-05-19. URL: <https://advacam.com/>.
- [30] B. Bergmann, T. Billoud, C. Leroy, and S. Pospisil. “Characterization of the Radiation Field in the ATLAS Experiment With Timepix Detectors”. In: *IEEE Transactions on Nuclear Science* 66.7 (2019), pp. 1861–1869. DOI: [10.1109/TNS.2019.2918365](https://doi.org/10.1109/TNS.2019.2918365).
- [31] D. Prelicpean. *Timepix3 radiation monitor at CNA - mono-energetic proton (alpha) beams ranging from 0.6 (1) to 5 (8.4) MeV*. Tech. rep. EDMS Report, 2024.
- [32] D. Prelicpean. *Timepix3 Radiation Monitor at CNA – 80 V Full Bias*. Tech. rep. EDMS Report, 2025.
- [33] H. Sandberg. *Development of a Novel Transverse Beam Profile and Emittance Monitor for the CERN Proton Synchrotron*. The University of Manchester (United Kingdom), 2020.
- [34] J. Gómez-Camacho, J. García López, C. Guerrero, et al. “Research facilities and highlights at the Centro Nacional de Aceleradores (CNA)”. In: *The European Physical Journal Plus* 136.3 (2021), p. 273. DOI: [10.1140/epjp/s13360-021-01253-x](https://doi.org/10.1140/epjp/s13360-021-01253-x). URL: <https://doi.org/10.1140/epjp/s13360-021-01253-x>.
- [35] S. P. George, M. Kroupa, S. Wheeler, S. Kodaira, H. Kitamura, L. Tlustos, T. Campbell-Ricketts, N. N. Stoffle, E. Semones, and L. Pinsky. “Very high energy calibration of silicon Timepix detectors”. In: *JINST* 13.11 (2018), P11014. DOI: [10.1088/1748-0221/13/11/P11014](https://doi.org/10.1088/1748-0221/13/11/P11014). URL: <https://cds.cern.ch/record/2654554>.
- [36] P. Schleper. *Particle Interactions with Matter*. University of Hamburg, DESY, 2018. URL: [https://www.desy.de/~schleper/lehre/Det\\_Dat/SS\\_2018/01\\_lecture\\_interaction\\_radiation\\_matter\\_1-14.pdf](https://www.desy.de/~schleper/lehre/Det_Dat/SS_2018/01_lecture_interaction_radiation_matter_1-14.pdf).
- [37] M. Sacristán Barbero, I. Slipukhin, M. Cecchetto, D. Prelicpean, Y. Aguiar, K. Bilko, N. Emriskova, A. Waets, A. Coronetti, M. Kastriotou, et al. “Characterization of Fragmented Ultra-high Energy Heavy Ion Beam and its Effects on Electronics Single Event Effect Testing”. In: *IEEE Transactions on Nuclear Science* (2024).

- [38] S. M. Abu Al Azm, G. Chelkov, D. Kozhevnikov, A. Guskov, A. Lapkin, A. Leyva Fabelo, P. Smolyanskiy, and A. Zhemchugov. “Response of timepix detector with GaAs:Cr and Si sensor to heavy ions”. In: *Physics of Particles and Nuclei Letters* 13 (May 2016), pp. 363–369. DOI: [10.1134/S154747711603002X](https://doi.org/10.1134/S154747711603002X). URL: <https://doi.org/10.1134/S154747711603002X>.
- [39] ALICE Collaboration. “The ALICE Experiment at the CERN Large Hadron Collider”. In: *JINST* 3 (2008), S08002. DOI: [10.1088/1748-0221/3/08/S08002](https://doi.org/10.1088/1748-0221/3/08/S08002).
- [40] N. Stoffle et al. “Timepix-based radiation environment monitor measurements aboard the International Space Station”. In: *Nuclear Instruments and Methods in Physics Research Section A: Accelerators, Spectrometers, Detectors and Associated Equipment* 782 (2015), pp. 143–148. ISSN: 0168-9002. DOI: <https://doi.org/10.1016/j.nima.2015.02.016>. URL: <https://www.sciencedirect.com/science/article/pii/S0168900215001977>.
- [41] ATLAS Collaboration. “The ATLAS Experiment at the CERN Large Hadron Collider”. In: *JINST* 3 (2008), S08003. DOI: [10.1088/1748-0221/3/08/S08003](https://doi.org/10.1088/1748-0221/3/08/S08003).
- [42] LHCb Collaboration. “The LHCb Detector at the CERN Large Hadron Collider”. In: *JINST* 3 (2008), S08005. DOI: [10.1088/1748-0221/3/08/S08005](https://doi.org/10.1088/1748-0221/3/08/S08005).
- [43] K. Akiba et al. “LHCb VELO Timepix3 telescope”. In: *Journal of Instrumentation* 14.05 (May 2019), P05026. DOI: [10.1088/1748-0221/14/05/P05026](https://doi.org/10.1088/1748-0221/14/05/P05026). URL: <https://dx.doi.org/10.1088/1748-0221/14/05/P05026>.

# List of Abbreviations

**CERN** European Organization for Nuclear Research

**SY** Systems

**STI** Sources, Targets and Interactions

**BMI** Beam Machine Interactions

**R2E** Radiation to Electronics

**LHC** Large Hadron Collider

**CNA** Centro Nacional de Aceleradores

**ASIC** Application Specific Integrated Circuit

**ToT** Time over Threshold

**ToA** Time of Arrival

# Acknowledgments

The biggest heartfelt gratitude goes to my supervisor **Dr. DANIEL PRELIPCEAN**, for giving me this golden opportunity that has shaped my whole career. Thank you for your continuous support and encouragement; great physicists and amazing people like you inspire me the most. Never ever will I forget your belief in me.

Great appreciation goes to my supervisor **Prof. Dr. VEIT WAGNER**, for his valuable guidance and dedication, not only on this thesis but also throughout my entire university journey over the past 3 years. I would also like to thank **Prof. Dr. ARNULF MATERNY**, for his nominations, constant support, and genuine positivity.

Deep gratitude towards all the professors and friends at Constructor University, and my truest lifelong friends whom I met in high school.

In closing, with great importance:

"Me gjithë zemër dua të falenderoj familjen time për dashurinë dhe mbështetjen e vazhdueshme. Babain tim **ALTIN REVANI** i cili e meriton autorësinë e kësaj diplome dhe titullin shkencëtar në vendin tim. Nënëen time **SONILA REVANI** e cila me shpirtin e saj të mirë më ka mësuar si të jem e lumtur dhe mirënjohëse për çdo gjë në jetë. Vëllain tim **ERNESTO REVANI** që ma bën jetën më të bukur dhe më kujton se nuk jam kurrë vetëm."

Kjo arritje është e juaja po aq sa është e imja.

"For I know only one thing; that I know nothing" -*Socrates*-